

1 **Textural and chemical features of a “soft” plug emitted during strombolian explosions: a case**
2 **study from Stromboli volcano**

3 A. Caracciolo^{1,2,3}, L. Gurioli², P. Marianelli³, J. Bernard^{2,4}, A. Harris²

4 Corresponding author: alberto@hi.is

5 1. Institute and Faculty of Earth Sciences, University of Iceland, Sturlugata 7, 101 Reykjavik, Iceland

6 2. Laboratoire Magmas et Volcans, Université Clermont Auvergne - CNRS - IRD, OPGC, Campus
7 Universitaire des Cézeaux, 6 Avenue Blaise Pascal, TSA 60026 - CS 60026, 63178 AUBIERE Cedex,
8 France

9 3. Dipartimento di Scienze della Terra, Università di Pisa, via Santa Maria 53, 56126 Pisa, Italy

10 4. Bureau de Recherche Géologique et Minière (BRGM), UMR 7327, 3 avenue Claude Guillemin,
11 BP 36009, 45060 Orléans Cedex 2, France

12

13 **Abstract**

14 Between May 2009 and March 2010, six small scale paroxysms were recorded at Stromboli volcano
15 (Aeolian Islands, Italy). The small scale paroxysm of 21 January 2010 was the only one characterized
16 by a SSE to SW dispersal direction, which allowed access for sampling of the associated bomb-
17 dominated deposit. The quenched marginal portions of twelve bombs were used to perform density,
18 textural and chemical analyses to define the mechanisms operating in the shallow conduit during the
19 explosion. Whole-rock density values span a range of 1100 to 2300 kg/m³ which, using a dense rock
20 equivalent density of 2850 kg/m³, converts to a vesicularity of 20 to 61 %. The vesicle volume
21 distribution (VVD) is unimodal, with a mode at 1.8 mm, consistent with a single bubble nucleation
22 event followed by growth, coalescence expansion and/or densification. Crystallinity ranges from 30-
23 62 vol. %. Vesicle and crystal contents, however, show considerable variation, consistent with the
24 presence of an extremely dense and degassed component in the fragmented magma. Both groundmass

25 glasses and melt inclusions are chemically homogenous, with CaO/Al₂O₃ in the range 0.40-0.60. Melt
26 inclusion volatile contents (H₂O up to 0.47 wt%) are consistent with fragmentation of a shallow
27 magma residing at a depth of about 480 m. We suggest that dense, degassed and crystal-rich magma
28 formed a “soft” rheological plug at the top of the conduit. Under such a condition, bubbles can
29 accumulate under the plug to slowly build the pressure to a threshold point, after which the pressure
30 is enough to cause the fragmentation of the plug.

31 **Key words:** Strombolian explosions, conduit-capping plug, degassed bombs, melt inclusions, small
32 scale paroxysms

33

34 **1. Introduction**

35 Stromboli, a 924 m high volcanic island located in the Aeolian archipelago of the Southern
36 Tyrrhenian Sea (Fig. 1), is famous for its persistent state of activity that has been on-going since the
37 medieval period (Rosi et al., 2000). All explosive eruptions occur in the crater terrace at 750 m a.s.l,
38 where the three main active craters are located (Fig. 1) (Harris and Ripepe, 2007a). Normal explosive
39 eruptions at Stromboli have been long-used to define the Strombolian sub-type of explosive activity
40 and typically involve 10²-10³ kg of material (Harris et al., 2013) in repeated emissions of gas, bombs,
41 lapilli and ash in events that last a few to tens of seconds (Barberi et al., 1993; Rosi et al., 2013;
42 Houghton et al., 2016). Because of the variety of the ejected material associated with explosive
43 events, normal activity at Stromboli has been subdivided in four main groups: type 0 events are gas
44 jets carrying a very few small particles at high velocity (Leduc et al., 2015; Gaudin et al., 2017); type
45 1 events are dominated by emission of ballistic coarse particles; type 2a eruptions involve ash-rich
46 plumes with large numbers of ballistics, and type 2b events are characterized prevalently by ash
47 (Patrick et al., 2007; Harris et al., 2013). Volcanic activity at the Crater Terrace also involves
48 continuous degassing (Pering et al., 2016) and gas puffing (Ripepe et al., 1996; Harris and Ripepe,
49 2007a; Gaudin et al., 2017), as well as emission of lava flows (e.g. Calvari et al., 2008; Rosi et al.
50 2013). The explosive plumes associated with normal activity ascend to no more than 500 m, causing

51 a discontinuous deposit of lapilli, bombs and/or coarse ash within 50-400 m of the vent (Harris and
52 Ripepe, 2007a; Patrick et al., 2007; Rosi et al. 2013; Gurioli et al., 2014). This activity has typically
53 been associated with the bursting of large bubbles of gas at the surface of the magma column (Parfitt,
54 2004) to expel a mixture of gas loaded with particles (Bombrun et al., 2015). Thus, while Stromboli
55 itself has become synonymous with this mildly explosive, yet globally common, eruption style,
56 fragmentation conditions and shallow conduit dynamics at Stromboli have also become intimately
57 linked to those driving “Strombolian” activity.

58 Recently, the simple Strombolian eruption model whereby large slugs of gas ascend through
59 liquid resident in the conduit to burst at the surface (Jaupart and Vergnolle, 1989) has been
60 challenged due to the presence of ejecta with moderate-to-high crystallinity. While pyroclasts at
61 Stromboli have 40 to 55 vol% of crystals (Métrich et al., 2010; Gurioli et al. 2014), those at Etna have
62 >55 vol% (Polacci et al., 2006), and crystallinities of 30-40 vol% have been found at Yasur volcano,
63 Vanuatu (Métrich et al., 2011). These crystal contents create rheological conditions that are close to
64 the “eruptibility” limit for magmas (Marsh 1981). The presence of a highly viscous (10^5 - 10^6 Pa s),
65 crystal-rich magma has thus motivated the generation of new models to explain the passage of the
66 slug through a more complicated system of liquid and solids (Gurioli et al. 2014; Oppenheimer et al.,
67 2020). At Stromboli, Gurioli et al. (2014) described two quenched bombs where fresh magma was
68 mingled with batches of degassed, oxidized, microlite-rich and evolved magma with high viscosity
69 and crystallinity. They hypothesized that this stagnant and oxidized magma formed a rheological
70 layer at the top of the magmatic column through which the fresh magma burst. Textural modeling
71 and geophysical analysis confirmed that the presence of this high density, high viscosity magma layer
72 modulates the type of emission during normal activity (e.g. Lautze et al. 2005; Leduc et al. 2015;
73 Gaudin et al. 2017). This layer could be related to the presence of debris on top of the vent (Patrick
74 et al., 2007; Capponi et al., 2016) and/or the presence of a plug made up of cooled, degassed and
75 partially crystallized magma at the top of the column (Capponi et al., 2016; Del Bello et al., 2015;
76 Lautze and Houghton, 2007; Oppenheimer et al., 2020; Suckale et al., 2016).

77 Small and large scale paroxysms punctuate persistent activity at Stromboli on annual and
78 decadal time scales (Rosi et al., 2013). Also termed “major explosions” (Barberi et al., 1993;
79 Bertagnini et al., 1999; Harris and Ripepe, 2007b), small-scale paroxysms consist of events involving
80 10^4 - 10^5 kg of material, have a duration of around a minute (Gurioli et al., 2013), and are accompanied
81 by short-lived plumes reaching a height of about 1 km (Rosi et al., 2013). They cause discontinuous
82 ballistic fallout within a distance of 500 m (Gurioli et al., 2013), and ash fall to the coast (1.5 km
83 distant) and beyond (Andronico and Pistolesi, 2010). Large scale paroxysms (Rosi et al., 2013)
84 involve 10^6 - 10^7 kg of material (Rosi et al., 2006) and are the most powerful eruptive events recorded
85 historically at Stromboli (Barberi et al., 1993; Bertagnini et al., 2011). They last several minutes and
86 can send meter-sized bombs and blocks up to 2 km from the craters, with the concurrent formation
87 of a convective plume that can ascend several kilometers (up to 10 km) above the vents (Pistolesi et
88 al., 2008; Rosi et al., 2013). These larger events have been explained as having a deeper trigger than
89 normal explosions. Eruptive dynamics during paroxysms is believed to be controlled by ascent of a
90 deep-seated, volatile-rich, magma that mingles with a degassed magma residing in the shallow
91 reservoir (Métrich et al., 2010).

92 Although spanning five orders of magnitude in terms of erupted mass, the small and large
93 scale paroxysms appear to be associated with the same near-surface conduit dynamics as normal
94 explosions, where the point of fragmentation is just a few 10’s to 100’s of meters below the vent
95 (Ripepe and Harris, 2008). For some small scale paroxysms, partial plug obstruction has been
96 observed and invoked as a trigger mechanism (Calvari et al., 2012). Calvari et al. (2014) also
97 suggested that, between 2007 and 2012, the geometry of the upper portion of the system evolved by
98 developing into a wide collapse depression that consumed the uppermost conduit, and which then
99 became refilled by partially melted hot debris and scoria (Del Moro et al., 2013). These structural
100 changes modified the shallow feeder conduit allowing a greater volume of magma to be stored and
101 degas at quasi equilibrium conditions, a volume which stays hotter for longer, enhancing the

102 possibility for the degassed magma to mingle with the deep-seated magma and increase the number
103 of small scale paroxysms (Calvari et al. 2014).

104 Within this framework of current understanding of Strombolian activity, we present results
105 from an interdisciplinary study in which we are able to texturally and chemically characterize the
106 magma sitting at the top of the shallow conduit at Stromboli, as emitted during a small scale paroxysm
107 that occurred on 21 January 2010. Our aim is to investigate the possible role of this magma in the
108 formation of a plug during more energetic Strombolian (small scale paroxysms) eruptions. The work
109 is based on complete mapping of an entire bomb-field associated with a small scale paroxysmal tied
110 to detailed sampled to generate a unique data set of bombs, collected for the first time from a single
111 bomb field emitted during a small scale paroxysm at Stromboli. We show that these bombs represent
112 a window into the character of Stromboli's conduit allowing us to define the nature of the shallow
113 magma associated with small scale paroxysms. We find that, for the small scale paroxysm sampled
114 here, a dense and crystal-rich plug at the top of the conduit controlled the eruption style, a finding
115 which links the genesis of small scale paroxysmal Strombolian explosions to that of normal activity.

116

117 **2. Stromboli magmatic system and textural features**

118 Stromboli volcano exhibits a wide range of explosive styles which reflect differences in the
119 magma involved. Normal activity and effusive events are fed by a crystal-rich and volatile-poor high
120 porphyritic (HP) magma (Bertagnini et al., 2008, 1999; Francalanci et al., 2004, 1999; Landi et al.,
121 2008; Métrich et al., 2010, 2001). HP magma contains 45-55 vol% of plagioclase (0.1-2.5 mm),
122 clinopyroxene (0.5-5 mm) and olivine (0.1-4 mm) in equilibrium with a shoshonitic residual melt
123 (~52 wt % SiO₂ and ~4.5 wt% K₂O). This magma is emitted as black scoriae. Different textural facies
124 have been described for HP scoriae associated with normal activity (Andronico et al., 2008; Belien
125 et al., 2010; Colò et al., 2010; Gurioli et al., 2014; Lautze and Houghton, 2008, 2007, 2005; Leduc et
126 al., 2015; Polacci et al., 2006) and a review of all published data is given in Table C1.

127 During large, as well as in some small scale paroxysms, in addition to HP magma, a crystal-
128 poor and volatile-rich melt is erupted, this being low porphyritic magma (LP, Table C1) (Bertagnini
129 et al., 2008, 1999; Francalanci et al., 2004, 1999; Métrich et al., 2010, 2001; Pioli et al., 2014). LP
130 magma is rarely released as pure “golden pumice” even in ash and fine lapilli size and is often variably
131 mingled with the HP magma (Pioli et al. 2014). LP magma contains the same mineral phases present
132 in HP scoriae, although plagioclase is lacking as phenocrysts. Crystallinity is also lower (<5 vol%)
133 in respect to the black scoria, and the LP groundmass glass has a basaltic composition (~48 wt %
134 SiO₂ and ~2.5 wt% K₂O) (Bertagnini et al., 1999; Francalanci et al., 2004; Rosi et al., 2013).

135 Stromboli’s plumbing system has become envisioned as a polybaric multi-reservoir system
136 (Métrich et al., 2010; Pichavant et al., 2011; Pompilio et al., 2012), consisting of: (i) a shallower
137 reservoir (~2 km) where the HP magma resides, (ii) a deep ponding zone at 7-10 km occupied by LP
138 magma, and (iii) a complex transition zone between the two, possibly characterized by a crystal mush
139 zone periodically influenced by ascending LP magma (Francalanci et al., 2004, 1999; ; Métrich et al.,
140 2010). With this in mind, the HP magma most likely derives from LP magma through crystallization
141 driven by decompression and water exsolution at low pressure (Métrich et al. 2001).

142

143 **3. The small scale paroxysm of 21 January 2010**

144

145 At 20:45:03 (local time) on 21 January 2010, thermal, infrasonic and seismic sensors of the University
146 of Florence (Italy) recorded a strong explosion at Stromboli. This small scale paroxysm lasted 51
147 seconds, consisted of three main phases, and was described in detail by Gurioli et al. (2013). The
148 explosion occurred after few days of crater inactivity. Following the reconstruction of Gurioli et al.
149 (2013), Phase 1 comprised two simultaneous bursts which sent bombs to the S/SSE and SW. Each
150 burst comprised two components: a leading spray of smaller bombs quickly followed by emission of
151 larger bombs that attained lower heights and fell closer to the vent than those of the first burst. An
152 associated cloud of gas and scarce finer material was observed, mostly connected to the SW-directed

153 burst and directed at an angle of 45°. The second phase began after seven seconds and involved
154 emission of two or three plumes of gas and scarce fine particles, lacking bombs. Phase 2 was
155 effectively over within 20 seconds and was followed by a third phase marked by a series of weakening
156 gas-rich puffs that lasted 24 seconds. Bombs were characterized by launch velocities between 52 and
157 70 m/s and the total erupted bomb mass was 3.6×10^4 kg, with bomb mass emission rates being
158 around 2×10^4 kg s⁻¹ (Gurioli et al., 2013). Fine fragments were indistinguishable and/or minimal
159 across the deposit (only one coarse lapilli was found), and sedimentation from phases 2 and 3
160 produced no distinguishable layer in more distal locations, as instead was observed for the small scale
161 paroxysm of 24 November 2009 (Andronico and Pistolesi, 2010).

162

163 **4. Sampling and analytical methods**

164

165 *4.1 Sample collection*

166 Samples studied in this work were mapped and collected during two sampling campaigns: one in June
167 2010 and another in June 2011 (6 and 18 months after the January 2010 eruption that emplaced the
168 sampled bombs). In total, 780 bombs were mapped (Fig. 1) and 55 bombs representative of the deposit
169 were sampled, in June 2010, along the longitudinal and horizontal dispersal axis (Fig.1, Gurioli et al.,
170 2013) every ten meters. As explained by Gurioli et al. (2013), the thermal video of the 21 January
171 event revealed bombs moving away from the camera, indicating a southward dispersal direction
172 opening at an angle of 180° (Fig. 1). Within this expected landing distribution, we mapped the SSE-
173 and the SW-directed bursts (Fig. 1). This means that the small scale paroxysm of 21 January 2010
174 was the source of the bombs, because it was the only explosion of the series of six small scale
175 paroxysms events that occurred between May 2009 and May 2010 with such a dispersal direction.
176 This distribution was confirmed by checking of thermal video for all six small scale paroxysms that
177 occurred during 2009-2010 (cf. Table 1 of Gurioli et al., 2013). The bomb field of 24 November 2009
178 had a southeast dispersion axis (Andronico and Pistolesi, 2010). This field overlaps that of 21 January

179 2010 to the east, but the majority of these bombs (purple diamonds in Fig. 1) can be distinguished
180 based on their larger size and on photos taken before and after the 21 January 2010 explosion (see
181 Item DR1, in Gurioli et al. 2013). All measured and collected bombs from the January 2010 event
182 were fresh, glassy and iridescent, and stratigraphically above older pyroclasts—a characteristic that,
183 even after 18 months, allowed them to be easily distinguished. Furthermore, all bombs were
184 photographed, measured (for long and short axis) and GPS-located during the June 2010 campaign,
185 allowing them to be relocated with confidence during the June 2011 campaign, when the dispersion
186 map was better defined and further morphological measurements of the bombs were made.

187

188 *4.2 Density and textural measurements*

189 For the 55 bombs sampled by Gurioli et al. (2013), densities were measured both as bulk density of
190 the entire bomb (Figs. 2A-F and Table C3 in Appendix C) and as density of the marginal portion of
191 the bomb (including quenched rind and some portion of the bomb, see limits of the thin section areas
192 Figs. A1 to A6 in Appendix A). Density was measured by comparing the sample weight in water with
193 the sample weight in air. While bomb rinds were made impermeable using Parafilm™ wax, bulk
194 bomb (which were larger than 8-10 cm) density measurements were carried out following the “natural
195 waterproofing” strategy (Gurioli et al., 2015). We measured the weight of the bombs in water using
196 the apparatus of Fig. 2G. The quenched rind prevented the water from entering the interior, as
197 confirmed by the lack of bubble formation in the water and the constant weight of the bomb before
198 and after immersion. After these measurements, bombs were cut into two slices along the major axis
199 and thin sections prepared from the marginal portions of 12 samples. Vesicularity (Φ) was determined
200 using the dense rock equivalent (DRE) density of 2850 kg/m^3 , as measured by Pistolesi et al. (2011).

201 Textural measurements, both for vesicles and crystals, were performed on 12 bombs following
202 the technique of Leduc et al. (2015). Images of sliced bombs and thin sections were acquired using a
203 desktop scanner, while the JEOL JSM-5910LV scanning electron microscope (SEM) at Laboratoire
204 Magmas et Volcans (LMV) in Clermont-Ferrand (France) was used for larger magnification images.

205 Each image was adjusted in Adobe Photoshop (e.g., broken bubble walls were connected) and
206 processed using the Fast Object Acquisition and Measurement System (FOAMS) software of Shea et
207 al. (2010). From each image, vesicles (black), crystals (white) and glass (gray) were extracted (Fig.
208 B1, Appendix B). Percentage of vesicles and crystals were then measured (Table 1) and vesicle
209 volume plots created (Fig. B2). Our CSD plots represent the distribution of all mineral species: we
210 assumed that plagioclase crystals dominate the microphenocrysts and microlites range, while
211 clinopyroxene and olivine crystals rule the phenocrysts population (see Figure B5).

212

213 *4.3 Geochemical analysis*

214 Chemical analysis of groundmass glasses, phenocrysts and melt inclusions (MI) were carried out
215 using the Philips XL30 SEM at the Dipartimento di Scienze della Terra (DST, Università di Pisa,
216 Italy) integrated with an energy-dispersive X-ray spectroscopy (EDS) which employs the EDAX-
217 DX4 software. Operating conditions were a 20 kV voltage and a 0.1 nA beam current. A raster area
218 of 100 μm^2 was employed for glass analysis to reduce light element loss. A set of reference standard
219 of natural trachytic (CFA47), basaltic (ALV981R23) and pantelleritic (KE12) glasses was analyzed
220 before each session. Major element composition of the groundmass glasses was analyzed using the
221 electron microprobe (EMP), SX-100 CAMECA, at LMV. Operating conditions were an accelerating
222 voltage of 15 kV and a defocused beam with an 8 nA current intensity. A comparison between EDS
223 and EMPA analysis is reported in Table C5.

224 Phenocrysts were hand-picked, mounted on slides and double polished. After petrographic
225 inspection, selected melt inclusions were prepared for volatile measurements. H_2O and CO_2 were
226 analyzed by transmission IR spectroscopy (FTIR) using a Nicolet iN10 equipped with a high-intensity
227 EverGlo IR source and a MCT-A detector cooled with liquid nitrogen at DST. Concentrations were
228 calculated according to the Beer-Lambert law: $C = \text{Abs} \times \text{PM} / \varepsilon \times \rho \times d$, where Abs is the absorbance,
229 PM the molar mass (g/mol), ε the molar absorptivity (L/mol-cm), ρ the MI density (kg/m^3) and d the
230 MI's thickness (cm). Melt density was calculated by major element composition (average 2630

231 kg/m³) and thickness of each sample was measured using a calibrated optical microscope. All the
232 measured and calculated Beer-Lambert parameters are given in table C2.

233

234 **5. Results**

235

236 *5.1 Macroscopic description and density analysis*

237 All sampled bombs are uniformly black with dimensions ranging from 5 to 44 cm, the smallest clast
238 being the only coarse lapilli found and sampled across the bomb field (Figs. 2A to 2E and Figs. A1
239 to A6,). Most have a quenched rind (Figs. 2B, 2D and 2E) of variable thickness (4-18 mm) which is
240 rich in crystals and small vesicles (e.g. S20 in Fig. A1 and A7 in Fig. A5,), while slightly larger
241 vesicles are normally clustered, more or less homogeneously, in the interior of the bomb (Fig. 2).
242 Occasionally, the central portion of the bomb is characterized by a large, centimetric void (Fig. 2E).
243 The occurrence of this difference between the marginal portion and the center is more marked for the
244 highly vesicular samples, while some of the densest bombs lack such a difference (Fig. 2 and Figs
245 A1 to A6,). However, even in the vesiculated samples, poorly-vesiculated areas are scattered across
246 the whole bomb surface. All bombs are scoriaceous apart from one (Fig. 3A), which contains an
247 elongated, light toned, vesicle-rich and crystal-poor pumice zone, typical of LP magma. The contact
248 between the pumiceous and scoriaceous zone is sharp and well-defined near the bomb's outer edge,
249 but irregular towards the interior (Fig. 3A).

250 Densities for all of the 55 samples have a Gaussian trend, with density values in the range of
251 1100 to 2300 kg/m³ (Fig. 2F and Table C3). Similarly, the marginal portion samples (the cut for the
252 thin sections) record narrower density range (1140-2050 kg/m³). Density values for the marginal
253 portion are always lower than the correspondent values for the whole bombs (Table 1).

254

255

256 *5.2 Textural data*

257 For the twelve analyzed bombs, porosity decreases as the number of large, coalesced, centimetric to
258 millimetric vesicles decreases (Table 1 and A1-A6; Figs. 4D, 4E and 4F). In contrast, the number of
259 small vesicles (<50 μm in diameter), which are typically rounded (Fig. 4E), increases as bomb density
260 increases. The LP facies differs from the HP facies within the same scoria sample, mostly because of
261 its very high vesicularity, with a population of rounded, small to medium sized vesicles that are
262 normally organized in chains (Fig. 4C).

263 The simplest vesicle volume distribution histograms (VVDs, Fig. 5A-D) display unimodal,
264 symmetrical distributions, with vesicles ranging from 0.03 to 18 mm and a mode value at around 1.8
265 mm. More complex VVD histograms are characterized by negative or positive asymmetrical
266 distributions with the same modes at 1.8 mm or finer modes at 1.3 or 0.7 mm (Fig. B2). Only for
267 A23, S20 and S28 a bimodal distributions is present due to a second coarse population around modes
268 of 4, 7 or 17 mm (Fig. B2). VVDs for whole bombs (in black in Figs. 5A-C and B2) and marginal
269 portions (in grey in Figs. 5A-C and B2) are very similar, although the marginal portions are always
270 more vesicular than the corresponding whole bomb. Only the LP texture (Fig. 5D) is different, having
271 a much greater vesicularity (67 %) and a unimodal, symmetrical distribution. This latter distribution
272 is due to the lack of large vesicles and abundance of small vesicles with a main mode at around 0.5
273 mm (Fig. 3C and Fig. 5D). In agreement with Polacci et al. (2009, 2006) and Cigolini et al. (2008),
274 corrected vesicle number density (N_v^{corr}) values are of the order of magnitude of 10^2 and 10^3 mm^{-3} ,
275 with the LP texture having the greatest value (Table 1). Some of the densest scoria also have relatively
276 high values of N_v^{corr} due to an increase of small vesicles in respect to the more porous scoria (Fig. 4
277 and Table 1).

278 Bombs have a crystal assemblage that comprises plagioclase, clinopyroxene and olivine (Fig.
279 4A) in a uniform glassy groundmass (Fig. 4B). Also in agreement with Cigolini et al. (2008) and Pioli
280 et al. (2014), crystallinity corrected for vesicularity ranges from 30 to 63 vol. % for the scoria, but for
281 the LP texture the crystal content is just 1.7 vol. %, (Table 1). Crystallinity is correlated with
282 vesicularity, with the least dense bombs having the highest crystal contents (Table 1). The whole

283 CSDs are very similar among all samples (Fig. 5E and Fig. B3-B4), where crystal sizes range from
284 50 μm to 14 mm. The CSD curves can be divided into three portions defined by different slopes.
285 Based on the whole CSD population size (Fig. 5G-H and B3-B4), we defined phenocrysts as crystals
286 with long axes of more than 350 μm , microphenocrysts with long axes between 100 and 350 μm , and
287 microlites with long axes less than 100 μm ; where microlites and microphenocrysts are mostly
288 formed by plagioclase.

289

290 *5.3 Groundmass glass and mineral chemistry*

291 At the microscale (thin section), the groundmass glass of scoriae appears dark or light brown,
292 although different colors do not correspond to differences in chemical composition, as already proved
293 by Leduc et al. (2015). The chemical homogeneity of the glass is apparent in the major element oxide
294 frequency diagrams (Figs. 6 and 8A-B). The glass is basaltic trachyandesite ($\text{SiO}_2 \sim 53 \text{ wt\%}$ and
295 $\text{CaO}/\text{Al}_2\text{O}_3 \sim 0.49$) with a shoshonitic character ($\text{K}_2\text{O} > 4 \text{ wt\%}$) and its SiO_2 content overlaps the bulk
296 rock composition (Fig. 6B). Pumice glass is trachybasaltic in composition ($\text{SiO}_2 \sim 49 \text{ wt\%}$ and
297 $\text{CaO}/\text{Al}_2\text{O}_3 \sim 0.61$) and is distinguishable from scoria glass for MgO, FeO, TiO_2 , Al_2O_3 and K_2O
298 contents (Figs. 3B and 6). The groundmass glass has a maximum H_2O content of 1600 ppm. The bulk
299 rock composition of the bombs falls in the trachybasalt field (white star in Fig. 6A).

300 Plagioclase crystals show both homogeneous and zoned textures and they are in the range
301 $\text{An}_{61} - \text{An}_{83}$. Zoned plagioclases have sieved texture zones, with an An-rich cores (An_{83}) surrounded
302 by labradoritic rims. Unzoned plagioclases are in the range An_{61-70} . Pyroxene phenocrysts, normally
303 zoned, have diopsitic/augitic compositions, being in the range $\text{Mg}^{\#}_{73-89}$. Olivine crystals are
304 homogeneous and exhibit a narrow compositional range (Fo_{70-73}).

305

306 *5.4 Melt inclusions: petrography, major element and volatile composition*

307 Naturally-quenched, light brown, melt inclusions are widespread in plagioclase, olivine and
308 clinopyroxene crystals (Fig. 7). Plagioclase crystals contain small MIs which have been neglected in

309 our study due to their small size. Olivine and clinopyroxene crystals contain both small-sized (10-20
310 μm) and large-sized ($>100 \mu\text{m}$) MIs. The latter are mostly found in olivine crystals and they are
311 usually glassy without significant petrographic evidence of post-entrapment crystallization (Fig. 7A).
312 However, diffusive re-equilibration of the inclusion with its host can modify the composition of the
313 trapped melt, along with crystallization of olivine on the walls of the inclusion. Therefore, we
314 corrected olivine-hosted MI compositions for post-entrapment processes (PEP) using Petrolog 3.0.
315 Olivine-hosted MIs required PEP correction between 0-5%. Clinopyroxene-hosted MIs needed up to
316 16% post-entrapment dissolution of the host mineral back into the inclusion (Table C4). A selection
317 of raw and PEP-corrected MI compositions is reported in table C4. PEP-corrected MIs, which are
318 used in the subsequent discussion, are chemically homogenous and they exhibit a shoshonitic
319 character (Fig. 6), with a $\text{Na}_2\text{O}+\text{K}_2\text{O}$ around 7.5 wt%, overlapping the groundmass field. Indeed,
320 frequency histograms of major oxides (Fig. 8) highlight similar compositions for both MIs and
321 groundmass glasses, showing a modal value of oxides (e.g. K_2O and FeO) centered at the same
322 percentage. H_2O in MI ranges from 0.27-0.47 wt % (Table 2), while CO_2 content is below the
323 detection limit.

324 All of our data highlight a homogeneous chemical composition, with MgO between 2.8 and
325 5.8 wt% and $\text{K}_2\text{O}/\text{Na}_2\text{O}$ in the range 0.9-1.8 (Table 2), and fall within the HP glass field for normal
326 activity (Fig. 6B) (Leduc et al., 2015; Métrich et al., 2005; Pioli et al., 2014). Only the pumice
327 groundmass glass moves away from HP field (Fig. 3). A relation between MI and groundmass glass
328 both in HP (and LP) products is reported in Figure 6B, as a $\text{CaO}/\text{Al}_2\text{O}_3$ vs K_2O diagram. MIs show a
329 $\text{CaO}/\text{Al}_2\text{O}_3$ ratio around 0.40-0.60 and they plot in a field far away from MI from pumice of Pioli et
330 al. (2014) and Métrich et al. (2001; 2005). MIs, found in pumice clasts, display more primitive
331 features and they have a wide range of $\text{CaO}/\text{Al}_2\text{O}_3$, this being from 0.5 to up 1.0 (Fig. 6B).

332 Scoria bulk-rock chemistry is comparable with the pumice groundmass glass (Fig. 6), whereas
333 the scoriae groundmass can be derived from the whole rock composition by crystallizing ~ 55 wt%
334 plagioclase, clinopyroxene and olivine (Métrich et al., 2001), in accordance with our textural analysis

335 (Table 1). All of these points suggest that the trapped melt (i.e. MIs) can be assumed as representative
336 of the melt present in the conduit just before the explosion. Therefore, the volatile (H₂O and CO₂)
337 content can be used to infer the depth of the melt in the conduit. Using VolatileCalc 2.0 (Newman
338 and Lowenstern, 2002), we have estimated a minimum volatile saturation pressure of 13.5 MPa. This
339 estimated pressure, assuming a magma DRE of 2850 kg/m³ (Pistolesi et al., 2011), corresponds to a
340 depth of about 480 m.

341

342 **6. Discussion**

343

344 *6.1 Textural evidence for a degassed magma*

345 The marginal portions of the bombs have lower density values with respect to their parental bomb.
346 Usually this should be the inverse, because the external portions of a bomb should be quenched faster
347 than the internal portion and preserve a pristine texture where expansion and coalescence of vesicles
348 are impeded. In contrast, vesiculation (in terms of expansion and/or coalescence) and sometimes
349 crystallization, in the bomb interior, continues after emission, so processes of post-deposition
350 modification are prevalent (e.g., Fig. 2E). Therefore, post-fragmentation expansion and formation of
351 blisters at the center of a bomb should reduce the density values for the whole bomb over those of the
352 quenched surface. In our sample collection, only a few bombs have large gas blisters (Figure 2E), but
353 those quantified in this study (see photos in Appendix A) are not as expanded as they should have
354 been because we are dealing with gas-depleted magma. Only in a few bombs can we see concentration
355 of large vesicles, but we see no real vesicle gradient (samples S27, S20, A25, A7). The lack of a any
356 obvious expansion gradient, the lack of large vesicles and the presence of scattered, less vesiculated
357 areas, causes the whole bomb to be denser than the area covered by the thin section. However, all
358 bombs, even those with central blisters, belong to the high density (HD) class described by Lautze
359 and Houghton (2005) and have densities comparable with the highest values found by Gurioli et al.
360 (2014) (Table C1). This means that these products are truly degassed, so that the internal vesicles

361 could not have expanded to any significant extent. Generally, at Stromboli, post fragmentation
362 expansion features are more predominant in the scoria lapilli grain size (which are slightly richer in
363 gas in respect to bombs), resulting in an increase in clast density as the size of the pyroclast increases
364 (see Fig. 1 in Bombrun et al. 2015).

365 Low density material was not found across the bomb field (Gurioli et al. 2013) and there was
366 no evidence of distal sedimentation of fine material, as observed by Andronico and Pistolesi (2010)
367 for a small scale paroxysm at Stromboli in 2009. The degassed nature of the magma is borne out by
368 MI data, which suggests the occurrence of a degassed magma residing in the shallow system.
369 However, this magma (Fig. 6B) is not as microlite-rich and is not as evolved as the magma found by
370 Gurioli et al (2014). As explained by Gurioli et al (2014), bombs sampled during normal activity
371 undergo cooling, crystallization and oxidation because sit at the very top of the magmatic column,
372 being a thin rind at the free surface and therefore representing a very thin crust at the head of the
373 degassing magma column. In the 2010 small scale paroxysm sampled here, we did not find the
374 equivalent of such a thin conduit-capping “crust”. Based on our observations of the thermal video for
375 the 2010 event, we argue that this crust probably fell within 200 m of the vent where it was not
376 possible to sample. However, the degassed magma within the conduit, that was resident beneath the
377 cooling crust, was too hot to crystallize microlites or to undergo oxidation, although the zonation of
378 the plagioclase reveals a prolonged residence time within the shallow conduit (cf. Landi et al., 2004),
379 as does the reduction in vesicles in the high density products. This is also clear in Figure 2 where low
380 density bombs are associated with post-eruption vesicular gradients, which it is not the case for high-
381 density samples (Figs. 2b, 2d and 2e). These high-density bombs thus represent the physical
382 characteristics of the magma at the top of the column at the moment of the explosion.

383 VVDs are generally used to infer the condition of the bubbles in the magma at the time of
384 explosion if quenching is effective and post fragmentation can be excluded (Gurioli et al. 2018, 2015,
385 2014; Polacci et al. 2006). The single mode observed here is consistent with a single bubble nucleation
386 and growth event, while bimodal distributions have been observed only in the three samples having

387 the best evidenced of expansions and coalescence for the large vesicles. While large vesicles dominate
388 in relatively low-density bombs, small vesicles increase in number in the high-density products,
389 where coalescence is less visible. These features are consistent with Lautze et al. (2008, 2007, 2005)
390 and Gurioli et al. (2014) who found that the most outgassed material, which experiences a longer
391 residence time in the conduit relative to the traditional HP magma, was denser and lacked syn-
392 eruptive coalescence signatures. Following Belien et al. (2010), we can also ascribe the presence of
393 small-sized vesicles as being due to the influence of crystals. Crystal content is positively correlated
394 with the percentage of small-sized vesicles, where bubbles will deform and split during percolation
395 processes occurring in a steadily crystalizing mixture. All of these observations indicate that the
396 erupted bomb mass derived from a slowly degassing, crystallizing source sitting at the top of the
397 shallow system. Although emitted as part of a small scale paroxysm, the texture of the bombs suggests
398 a single stage of bubble nucleation and growth, typical of normal Strombolian activity (cf. Lautze and
399 Houghton, 2005; Polacci et al., 2006).

400 CSDs show similar relationships to those presented by Pioli et al. (2014). In Figure 5F we plot
401 CSD curves with the highest (black) and lowest (grey) crystallinities from Pioli et al. (2014),
402 Fornaciai et al. (2009) and this study. While normal activity samples (Fornaciai et al. 2009) show
403 linear trends, samples emitted during small scale paroxysms appear to correlate with crystallinity,
404 with low crystal frequencies at lower crystallinities, as also found by Pioli et al. (2014). Finally, the
405 small size interval of CSD curves can be affected by crystal fragmentation (Forien et al., 2011) which
406 would produce the observed exponential trends.

407

408 *6.2 Geochemical constraints and volatile-based estimates*

409 Our chemical data highlight the exclusive occurrence of a shoshonitic, chemically
410 homogeneous (HP) magma. Only the pumice groundmass glass moves away from the HP field and
411 its chemistry is consistent with a deep-seated LP magma as defined by Métrich et al. (2010). A
412 distinction between HP and LP glass is clearly shown in Figure 3B, where we report a geochemical

413 transect across the HP-LP-HP facies. The two melts are distinguishable especially at the edge between
414 the scoria and the pumice, where the LP glass has a more primitive signature. The observed gap
415 between the composition of pumice and of scoria glass, together with the element frequency diagrams
416 (Fig. 8), allow us to rule out mingling processes down to a micrometric scale. Therefore we interpret
417 the “golden pumice” as a xenolith that was present at the top of the magmatic column before the
418 explosion, which was emitted during an earlier event and then recycled by the sampled event. Many
419 bombs were also broken in the field and did not show evidence of LP portions. Nevertheless, the LP
420 magma presence cannot be totally excluded, as we could not sample the very scarce finer material
421 visible in the explosions. Evidence of LP magma in coarse ash from normal activity has already been
422 well documented by D’Oriano et al. (2011). Thus, this small scale paroxysm appears to have involved,
423 and been driven by, an entirely HP magma.

424 The low volatile content of our glasses is consistent with a magma that has been free to degas,
425 and which has thus lost almost all of its H₂O and CO₂. From MI investigations we can thus assume
426 that MIs were trapped inside the shallow portion of the conduit above a depth of 500 m. This depth
427 corresponds at the zone where very long period (VLP) signals have been located during normal
428 through paroxysmal activity at Stromboli (Chouet et al., 2003; Ripepe and Harris, 2008; Gurioli et
429 al., 2014), reinforcing the MI-based pressure calculation and increasing the strength of the argument
430 posed by our data. We note, here, that the depth of the VLP has not been linked to the thickness of
431 any degassed layers, but instead has been related to a level at which gas coalescence may occur
432 (Ripepe et al. 2001; Chouet et al. 2003), at which a specific conduit geometry exists that promotes a
433 change to a bubbly flow regime (James et al. 2009), or where the last crystallization may occur, as
434 shown in this paper. Instead, considering the total mass of the deposit of 3.6×10^4 kg (Gurioli et al.,
435 2013) and a mean bomb bulk density of 1850 kg/m³, for a conduit diameter of 1 m (Vergnolle et al.,
436 1996), we can estimate the in-conduit thickness of the erupted, degassed HP magma to have been
437 approximately 25 m, in agreement with the length of the plug of 10-50 m estimated by Woitischek et
438 al. (2020). This would thus have contributed a 25 m thick layer at the head of a density-stratified

439 magma column above the VLP, with our data suggesting that crystallization is complete (or
440 completed) by the depth of the VLP.

441

442 *6.3 Implication for Strombolian eruptions*

443 The homogeneous nature of these bombs is in contrast with the hypothesis of a finger-like
444 system composed of a network of smaller volumes of different magma, as proposed in Calvari et al
445 (2014). In such a scenario we should have expected a more heterogeneous deposit with evidence of
446 non-juvenile materials stripped off from the explosion and mingling with the LP magma. The
447 presence of the LP magma involved as xenoliths can be consistent with a simpler, large storage
448 reservoir that allows more HP magma to accumulate and at the same time, preserve old magma left
449 behind by more energetic explosions.

450 Oppenheimer et al. (2020) investigated and modelled the physical interactions between
451 bubbles and crystals defining a “soft plug model” for Strombolian eruptions, in which large quantities
452 of crystals temporally impede and/or delay bubble ascent, with consequent bubble accumulation
453 under the plug increasing until the pressure exerted by this building accumulation becomes suddenly
454 released. The term “soft” is used for this kind of low-melt-viscosity plugs, that are equivalent to the
455 rheologically “stronger” plugs involved in Vulcanian-style eruptions (cf. Oppenheimer et al., 2020).
456 It is known that magma residing in the shallow conduit of Strombolian volcanoes are crystal rich,
457 with 30 to 60 vol%. This amount of crystals is responsible for the development of an effective yield
458 strength which favors bubble accumulation and subsequent local overpressure. We believe that the
459 21 January 2010 small scale paroxysm at Stromboli volcano is consistent with the fragmentation of
460 a dense and crystallized plug of magma residing in the upper part of the conduit. Fragmentation of
461 this 25 m thick plug resulted in the generation of a very coarse population of pyroclasts that ascended
462 the conduit and fed the resulting plume.

463 Our study thus shows that a “soft” plug control exists for Strombolian explosions, where
464 eruptive events involve crystal-rich magmas which form strong and poorly-permeable plugs

465 (Oppenheimer et al., 2020) through which ascending slugs must burst during both normal and
466 paroxysmal eruptions (cf. Gurioli et al., 2014). Possibly, for the small scale paroxysms, the change
467 in geometry of the upper feeding systems could have favored the accumulation of a relatively large
468 quantity of HP magma (Calvari et al. 2014). We here show that, in addition to the configuration of
469 the flow within the conduit (Capponi et al., 2016; Del Bello et al., 2015; Oppenheimer et al., 2020;
470 Suckale et al., 2016), the transition between different strombolian activity styles is controlled by the
471 presence of a crystal-supported stagnant magma sitting at the top of the magma column. This suggests
472 that a weak plug model is reasonable for “strombolian” systems characterized by moderate-to-high
473 crystallinities, as also observed for other strombolian-type eruptions such at Yasur, Villarrica and
474 Erebus volcano (Woitischek et al. 2020).

475

476 **7. Conclusion**

477 Recent work has shown that the shallow system at Stromboli is a highly dynamic environment
478 (Calvari et al. 2014) that experiences a continual change in the character and rheology of the resident
479 magma during normal explosive activity (D’Oriano et al., 2011; Lautze and Houghton, 2008, 2007;
480 Leduc et al., 2015). In this model, a degassed layer with high viscosity and yield strength (Gurioli et
481 al., 2014), or a “plug” (Calvari et al., 2012; Oppenheimer et al., 2020; Suckale et al., 2016), can form
482 and decay (Leduc et al., 2015). Suckale et al. (2016) argued for the presence of a porous plug of HP
483 magma beneath the entire crater terrace, made up of crystals, bubbles and melt, but with an overall
484 solid-like behavior. In this interpretation, normal eruptions are connected to the tensile failure of the
485 plug due to over-pressurization following build up, or arrival, of gas volumes at the base or within
486 the plug; failure of the plug then feeds the eruption during normal events (Gurioli et al., 2014). Our
487 data now indicate that some small scale paroxysms have a similar genesis, meaning that the model,
488 and process, scales-up.

489 Large, and some of the small, paroxysmal events at Stromboli have typically been considered
490 as associated with the ascent of deep-sourced LP magma (Andronico and Pistolesi, 2010; Cigolini et

491 al., 2015; Pistolesi et al., 2011). However, bombs sampled from the 21 January 2010 small scale
492 paroxysm show that this is not the case. Indeed, we find that no LP magma was involved, and that
493 the emission resulted from the fragmentation of a cap of degassed and dense HP magma. Thus, the
494 capping model invoked for normal explosions at Stromboli can be scaled up to small scale paroxysms
495 with a deformed flow regime (Oppenheimer et al., 2020) governing the ascent dynamic. In the case
496 of the small scale paroxysm examined here, the higher magnitude and energy (and thus also distance
497 reached by the bombs) is due to the formation of a plug when compared with normal explosions. The
498 period of inactivity at the crater involved (a few days) probably allowed the plug to form a cold crust,
499 obstructing the crater and promoting a larger explosion than normal. This finding strongly supports
500 that we need to review our mechanical model for Strombolian eruptions and move away from simple
501 foam collapse and bubble ascent speed models (e.g., Parfitt, 2004) in rheologically “clean” and simple
502 conduits, and move towards more complex models (Del Bello et al., 2015; Oppenheimer et al., 2020)
503 which consider strong rheological stratification effects due to near-surface crystallization processes.
504 Our findings thus support a new model whereby shallow conduit dynamics control the magnitude,
505 intensity and character of Strombolian explosions, even the more explosive events, where for all cases
506 the effect of a degassed, crystallized cap must be considered.

Acknowledgments

507 This research was financed by the French Government Laboratory of Excellence initiative n XXANR-
508 10-LABX-0006, the Région Auvergne, and the European Regional. This work was also supported by
509 the University of Pisa 2016 Ateneo funds and by the Erasmus + traineeship funding program from
510 Pisa University (Italy). We are thankful to Jean-Luc Devidal for assistance with EMPA analyses at
511 LMV and to Franco Colarieti for help with sample preparation at DST. We are very grateful to
512 Heather Handley for the editorial handling and we thank two anonymous reviewers for their
513 constructive suggestion that improved the quality of the manuscript.

Figure captions

514 **Figure 1.** Slope map of the summit crater area of Stromboli showing the location of mapped and
515 sampled bombs. Bombs studied in this work are shown in red. Inset: location map of Stromboli in
516 the Tyrrhenian sea.

517 **Figure 2.** Bomb slices of different size and density from the 21 January 2010 small scale paroxysm
518 at Stromboli. A) and C) Dense bombs without a quenched rind and with random vesicles
519 distribution; B) and D) Lighter bombs with a quenched marginal portions and a vesicularity
520 gradient; E) Bomb with a thick quenched rind and a large central vesicle, like a blister. F) Bulk
521 densities analysis of the 55 sampled bombs reported in a density vs sample frequency diagram. G)
522 Technique used to measure the bombs density. Samples were weighed considering a natural
523 waterproofing (Gurioli et al., 2015), measuring the weight before and after the immersion. No
524 weight changes have been measured on these values. ρ : bomb density

525 **Figure 3.** A.I) Bomb A25 containing an elongated golden pumice (red square). A.II) thin section
526 image of the pumice where it is specified the position of the chemical transect (dashed red line).
527 A.III) Electron back-scattered (BSE) image of the sharp contact (red line) between the HP magma
528 and the LP magma. B) Geochemical transect across the HP-LP-HP magma in a diagram distance
529 (μm) vs TiO_2 concentration. The two distinct melts are clear distinguishable especially at the edge
530 between the scoria and the pumice. This chemical distinction is also observed with other oxides as
531 MgO , FeO and Al_2O_3 .

532 **Figure 4.** Textural characteristics of the products from the 21 January 2010 small scale paroxysm at
533 Stromboli. A) Microscope image at polarized light showing the general mineral assemblage formed
534 by plagioclase, pyroxene and olivine. B) BSE image of the groundmass glass (light grey); in darker
535 grey are the plagioclase and in black the vesicles; C), BSE-SEM image of the vesicle-rich golden
536 pumice; D), E) and F) BSE images of scoria with different vesicularity.

537 **Figure 5.** Vesicle volume distributions (VVDs) and crystal size distribution (CSDs) for selected
538 samples. (A-C) VVDs for three selected scoria samples and (D) for the golden pumice in sample A25.
539 Each diagram is formed by a grey histogram (representative the texture of the marginal portions of
540 the bombs) and a black histogram (representative the texture of the whole bomb). The golden pumice
541 is in white and the distribution is characterized by a predominance of small-size vesicles. For each
542 sample, we indicate the vesicularity of the whole bomb (Φ_{bomb}) and of the marginal portions (Φ_{quen}).
543 (E) CSDs of all studied samples, in the crystal size interval 0-15mm. Single CSD curves are reported
544 in appendix B3 and B4. (F) CSDs of samples with the highest and lowest crystallinity from this study
545 and comparison with samples studied in Pioli et al. (2014) and Fornaciai et al. (2009). (G-H) CSD
546 curves in a restricted crystal size range (0-1.4 mm), showing the three crystals families (gray lines),
547 as microlites (<100 μm), microphenocrystals (100-350 μm) and phenocrystals (>350 μm).

548 **Figure 6.** Scoria groundmass glass analyses (red circles) and olivine- and pyroxene-hosted melt
549 inclusions (orange triangles) of scoria samples and pumice groundmass glass (yellow circles)
550 plotted in A) a TAS diagram and in B) CaO/Al₂O₃ vs K₂O/Na₂O diagram. Both groundmass glasses
551 and MI from scoriae show a shoshonitic composition. In the CaO/Al₂O₃ vs K₂O plot MIs and
552 glasses cluster in the Stromboli HP field. *LP and HP field of Stromboli MIs and groundmass
553 glasses are represented accordingly to Métrich et al. (2005, 2001) and Pioli et al. (2014). For
554 comparison, we also report the more evolved groundmass glass compositions (gray circles) found
555 by Gurioli et al. (2014).

556 **Figure 7.** (A-B) Transmission microscope images of naturally-quenched olivine-hosted melt
557 inclusions; (C-F) back scattered images of significant large-size MIs. MIs are glassy and fully
558 enclosed, without any significant post-entrapment transformation. For each olivine crystal we
559 indicate the forsterite (Fo) content. Cpx: clinopyroxene crystal included in the melt inclusion.

560 **Figure 8.** Variation histograms for FeO and K₂O in (A-B) groundmass glasses and (C-D) melt
561 inclusions. Histograms are unimodal and for each oxide we observe a main mode fixed at the same
562 value. This variation is also observed in term of MgO, FeO, Al₂O₃ and K₂O.

References

- 563 Andronico, D., Corsaro, R.A., Cristaldi, A., Polacci, M., 2008. Characterizing high energy
564 explosive eruptions at Stromboli volcano using multidisciplinary data: An example from the 9
565 January 2005 explosion. *J. Volcanol. Geotherm. Res.* 176, 541–550.
566 <https://doi.org/10.1016/j.jvolgeores.2008.05.011>
- 567 Andronico, D., Pistolesi, M., 2010. The November 2009 paroxysmal explosions at Stromboli. *J.*
568 *Volcanol. Geotherm. Res.* 196, 120–125. <https://doi.org/10.1016/j.jvolgeores.2010.06.005>
- 569 Barberi, F., Rosi, M., Sodi, A., 1993. Volcanic hazard assessment at Stromboli based on review of
570 historical data. *Bull. Volcanol.* 3, 173–187.
- 571 Belien, I.B., Cashman, K. V., Rempel, A.W., 2010. Gas accumulation in particle-rich suspensions
572 and implications for bubble populations in crystal-rich magma. *Earth Planet. Sci. Lett.* 297,
573 133–140. <https://doi.org/10.1016/j.epsl.2010.06.014>
- 574 Bertagnini, A., Coltelli, M., Landi, P., Pompilio, M., Rosi, M., 1999. Violent explosions yield new
575 insights into dynamics of Stromboli volcano. *Eos (Washington. DC).* 80, 2–8.
576 <https://doi.org/10.1029/99EO00415>
- 577 Bertagnini, A., Di Roberto, A., Pompilio, M., 2011. Paroxysmal activity at Stromboli: Lessons from
578 the past. *Bull. Volcanol.* 73, 1229–1243. <https://doi.org/10.1007/s00445-011-0470-3>
- 579 Bertagnini, A., Métrich, N., Francalanci, L., P., L., Tommasini S., Conticelli, S., 2008. Volcanology
580 and magma geochemistry of the present-day activity: constraints on the feeding system. In:
581 Calvari, S. Inguaggiato, S., Puglisi, G., Ripepe, M. Rosi, M. (Eds.), *Learning from Stromboli:*
582 *American Geophysical Union. Geophys. Monogr.* 182, 19–38.
583 <https://doi.org/10.1029/182GM04>
- 584 Bombrun, M., Harris, A.J.L., Gurioli, L., Battaglia, J., Barra, V., 2015. Anatomy of a Strombolian
585 eruption: Inferences from particle data recorded with thermal video Maxime. *J. Geophys. Res.*
586 *Solid Earth Res.* 120, 2367–2387. <https://doi.org/10.1002/2014JB011556>.Received

- 587 Calvari, S., Bonaccorso, A., Madonia, P., Neri, M., Liuzzo, M., Salerno, G., Behncke, B.,
588 Caltabiano, T., Cristaldi, A., Giuffrida, G., La Spina, A., Marotta, E., Ricci, T., Spampinato,
589 L., 2014. Major eruptive style changes induced by structural modifications of a shallow
590 conduit system: the 2007–2012 Stromboli case. *Bull Volcanol* (2014) 76:841 DOI
591 10.1007/s00445-014-0841-7
- 592 Calvari, S., Bttner, R., Cristaldi, A., Dellino, P., Giudicepietro, F., Orazi, M., Peluso, R.,
593 Spampinato, L., Zimanowski, B., Boschi, E., 2012. The 7 September 2008 Vulcanian
594 explosion at Stromboli volcano: Multiparametric characterization of the event and
595 quantification of the ejecta. *J. Geophys. Res. Solid Earth* 117, 1–17.
596 <https://doi.org/10.1029/2011JB009048>
- 597 Calvari, S., Inguaggiato, S., Puglisi, G., Ripepe, M., Rosi, M., 2008. *The Stromboli Volcano: An*
598 *integrated study of the 2002-2003 eruption.* John Wiley & Sons.
599 <https://doi.org/10.1029/GM182>
- 600 Capponi, A., James, M.R., Lane, S.J., 2016. Gas slug ascent in a stratified magma: Implications of
601 flow organisation and instability for Strombolian eruption dynamics. *Earth Planet. Sci. Lett.*
602 435, 159–170. <https://doi.org/10.1016/j.epsl.2015.12.028>
- 603 Chouet, B., Dawson, P., Ohminato, T., Martini, M., Saccorotti, G., Giudicepietro, F., De Luca, G.,
604 Milana, G., Scarpa, R., 2003. Source mechanisms of explosions at Stromboli Volcano, Italy,
605 determined from moment-tensor inversions of very-long-period data. *J. Geophys. Res. Solid*
606 *Earth* 108, ESE 7-1-ESE 7-25. <https://doi.org/10.1029/2002JB001919>
- 607 Cigolini, C., Laiolo, M., Bertolino, S., 2008. Probing Stromboli volcano from the mantle to
608 paroxysmal eruptions. *Geol. Soc. London, Spec. Publ.* 304, 33–70.
609 <https://doi.org/10.1144/SP304.3>
- 610 Cigolini, C., Laiolo, M., Coppola, D., 2015. Revisiting the last major eruptions at Stromboli
611 volcano: inferences on the role of volatiles during magma storage and decompression. *Geol.*

612 Soc. Spec. Publ. 410, 143–177. <https://doi.org/10.1144/SP410.3>

613 Colò, L., Ripepe, M., Baker, D.R., Polacci, M., 2010. Magma vesiculation and infrasonic activity at
614 Stromboli open conduit volcano. *Earth Planet. Sci. Lett.* 292, 274–280.
615 <https://doi.org/10.1016/j.epsl.2010.01.018>

616 D’Oriano, C., Bertagnini, A., Pompilio, M., 2011. Ash erupted during normal activity at Stromboli
617 (Aeolian Islands, Italy) raises questions on how the feeding system works. *Bull. Volcanol.* 73,
618 471–477. <https://doi.org/10.1007/s00445-010-0425-0>

619 Del Bello, E., Lane, S.J., James, M.R., Llewellyn, E.W., Taddeucci, J., Scarlato, P., Capponi, A.,
620 2015. Viscous plugging can enhance and modulate explosivity of strombolian eruptions. *Earth
621 Planet. Sci. Lett.* 423, 210–218. <https://doi.org/10.1016/j.epsl.2015.04.034>

622 Del Moro, S., Renzulli, A., Landi, P., La Felice, S., Rosi, M., 2013. Unusual lapilli tuff ejecta
623 erupted at Stromboli during the 15 March 2007 explosion shed light on the nature and thermal
624 state of rocks forming the crater system of the volcano. *J. Volcanol. Geotherm. Res.* 254, 37–
625 52. <https://doi.org/10.1016/j.jvolgeores.2012.12.017>

626 Forien, M., Arbaret, L., Burgisser, A., Champallier, R., 2011. Experimental constrains on shear-
627 induced crystal breakage in magmas. *J. Geophys. Res. Solid Earth* 116, 1–21.
628 <https://doi.org/10.1029/2010JB008026>

629 Francalanci, L., Tommasini, S., Conticelli, S., 2004. The volcanic activity of Stromboli in the 1906-
630 1998 AD period: Mineralogical, geochemical and isotope data relevant to the understanding of
631 the plumbing system. *J. Volcanol. Geotherm. Res.* 131, 179–211.
632 [https://doi.org/10.1016/S0377-0273\(03\)00362-7](https://doi.org/10.1016/S0377-0273(03)00362-7)

633 Francalanci, L., Tommasini, S., Conticelli, S., Davies, G.R., 1999. Sr isotope evidence for short
634 magma residence time for the 20th century activity at Stromboli volcano, Italy. *Earth Planet.
635 Sci. Lett.* 167, 61–69. [https://doi.org/10.1016/S0012-821X\(99\)00013-8](https://doi.org/10.1016/S0012-821X(99)00013-8)

636 Gaudin, D., Taddeucci, J., Scarlato, P., Del Bello, E., Ricci, T., Orr, T., Houghton, B.F., Harris,

637 A.J.L., Rao, S., Bucci, A., 2017. Integrating puffing and explosions in a general scheme for
638 Strombolian-style activity. *J. Geophys. Res. Solid Earth* 122, 1860–1875.
639 <https://doi.org/10.1002/2016JB013707>

640 Gurioli, L., Andronico, D., Bachelery, P., Balcone-Boissard, H., Battaglia, J., Boudon, G.,
641 Burgisser, A., Burton, M.R., Cashman, K. V., Cichy, S., Cioni, R., Di Muro, A., Dominguez,
642 L., D’Oriano, C., Druitt, T., Harris, A.J.L., Hort, M., Kelfoun, K., Komorowski, J.C.,
643 Kueppers, U., Le Pennec, J.L., Menand, T., Paris, R., Pioli, L., Pistolesi, M., Polacci, M.,
644 Pompilio, M., Ripepe, M., Roche, O., Rose-Koga, E.F., Rust, A., Schiavi, F., Scharff, L.,
645 Sulpizio, R., Taddeucci, J., Thordarson, T., 2015. MeMoVolc consensual document: a review
646 of cross-disciplinary approaches to characterizing small explosive magmatic eruptions. *Bull.*
647 *Volcanol.* 77. <https://doi.org/10.1007/s00445-015-0935-x>

648 Gurioli, L., Colò, L., Bollasina, Harris, A.J.L., Whittington, A., Ripepe, M., 2014. Dynamics of
649 Strombolian explosions: inferences from field and laboratory studies of erupted bombs from
650 stromboli volcano. *J. Geophys. Res. Solid Earth* 645–660.
651 <https://doi.org/10.1002/2013JB010264>.Received

652 Gurioli, L., Harris, A.J.L., Colò, L., Bernard, J., Favalli, M., Ripepe, M., Andronico, D., 2013.
653 Classification, landing distribution, and associated flight parameters for a bomb field emplaced
654 during a single major explosion at Stromboli, Italy. *Geology* 41, 559–562.
655 <https://doi.org/10.1130/G33967.1>

656 Harris, A.J.L., Delle Donne, D., Dehn, J., Ripepe, M., Worden, A.K., 2013. Volcanic plume and
657 bomb field masses from thermal infrared camera imagery. *Earth Planet. Sci. Lett.* 365, 77–85.
658 <https://doi.org/10.1016/j.epsl.2013.01.004>

659 Harris, A.J.L., Ripepe, M., 2007a. Temperature and dynamics of degassing at Stromboli. *J.*
660 *Geophys. Res. Solid Earth* 112, 1–18. <https://doi.org/10.1029/2006JB004393>

661 Harris, A.J.L., Ripepe, M., 2007b. Synergy of multiple geophysical approaches to unravel explosive

662 eruption conduit and source dynamics—a case study from Stromboli. *Geochem* 67, 1-35.
663 <https://doi.org/10.1016/j.chemer.2007.01.003>

664 Houghton, B.F., Taddeucci, J., Andronico, D., Gonnermann, H.M., Pistolesi, M., Patrick, M.R.,
665 Orr, T.R., Swanson, D.A., Edmonds, M., Gaudin, D., Carey, R.J., Scarlato, P., 2016. Stronger
666 or longer: Discriminating between Hawaiian and Strombolian eruption styles. *Geology* 44,
667 163–166. <https://doi.org/10.1130/G37423.1> James, M.R., Lane, S.J., Wilson, L., Corder, S.B.,
668 2009. Degassing at low magma-viscosity volcanoes: Quantifying the transition between
669 passive bubble-burst and Strombolian eruption. *J. Volcanol. Geotherm. Res.* 180, 81–88.
670 <https://doi.org/10.1016/j.jvolgeores.2008.09.002>

671 Jaupart, C., Vergnolle, S., 1989. The generation and collapse of a foam layer at the roof of a
672 basaltic magma chamber, *Journal of Fluid Mechanics*.
673 <https://doi.org/10.1017/S0022112089001497>

674 Landi, P., Métrich, N., Bertagnini, A., Rosi, M., 2008. Recycling and “re-hydration” of degassed
675 magma inducing transient dissolution/crystallization events at Stromboli (Italy). *J. Volcanol.*
676 *Geotherm. Res.* 174, 325–336. <https://doi.org/10.1016/j.jvolgeores.2008.02.013>

677 Landi, P., Métrich, N., Bertagnini, A., Rosi, M., 2004. Dynamics of magma mixing and degassing
678 recorded in plagioclase at Stromboli (Aeolian Archipelago, Italy). *Contrib. to Mineral. Petrol.*
679 147, 213–227. <https://doi.org/10.1007/s00410-004-0555-5>

680 Lautze, N.C., Houghton, B.F., 2008. Single explosions at Stromboli in 2002: Use of clast
681 microtextures to map physical diversity across a fragmentation zone. *J. Volcanol. Geotherm.*
682 *Res.* 170, 262–268. <https://doi.org/10.1016/j.jvolgeores.2007.10.011>

683 Lautze, N.C., Houghton, B.F., 2007. Linking variable explosion style and magma textures during
684 2002 at Stromboli volcano, Italy. *Bull. Volcanol.* 69, 445–460. [https://doi.org/10.1007/s00445-](https://doi.org/10.1007/s00445-006-0086-1)
685 [006-0086-1](https://doi.org/10.1007/s00445-006-0086-1)

686 Lautze, N.C., Houghton, B.F., 2005. Physical mingling of magma and complex eruption dynamics

687 in the shallow conduit at Stromboli volcano, Italy. *Geology* 33, 425–428.
688 <https://doi.org/10.1130/G21325.1>

689 Leduc, L., Gurioli, L., Harris, A.J.L., Colò, L., Rose-Koga, E.F., 2015. Types and mechanisms of
690 strombolian explosions: characterization of a gas-dominated explosion at Stromboli. *Bull.*
691 *Volcanol.* 77. <https://doi.org/10.1007/s00445-014-0888-5>

692 Marsh, B.D., 1981. On the crystallinity, probability of occurrence, and rheology of lava and magma.
693 *Contrib. to Mineral. Petrol.* 78, 85–98. <https://doi.org/10.1007/BF00371146>

694 Métrich, N., Bertagnini, A., Di Muro, A., 2010. Conditions of magma storage, degassing and ascent
695 at Stromboli: New insights into the volcano plumbing system with inferences on the eruptive
696 dynamics. *J. Petrol.* 51, 603–626. <https://doi.org/10.1093/petrology/egp083>

697 Métrich, N., Bertagnini, A., Landi, P., Rosi, M., 2001. Crystallization driven by decompression and
698 water loss at Stromboli volcano (Aeolian Islands, Italy). *J. Petrol.* 42, 1471–1490.
699 <https://doi.org/10.1093/petrology/42.8.1471>

700 Métrich, N., Bertagnini, A., Landi, P., Rosi, M., Belhadj, O., 2005. Triggering mechanism at the
701 origin of paroxysms at Stromboli (Aeolian Archipelago, Italy): The 5 April 2003 eruption.
702 *Geophys. Res. Lett.* 32, 1–4. <https://doi.org/10.1029/2004GL022257>

703 Newman, S., Lowenstern, J.B., 2002. Volatile Calc : a silicate melt – H₂O – CO₂ solution model
704 written in Visual Basic for excel. *Comput. Geosci.* 28, 597–604.
705 [https://doi.org/doi:10.1016/S0098-3004\(01\)00081-4](https://doi.org/doi:10.1016/S0098-3004(01)00081-4)

706 Oppenheimer, J., Capponi, A., Cashman, K. V., Lane, S.J., Rust, A.C., James, M.R., 2020.
707 Analogue experiments on the rise of large bubbles through a solids-rich suspension: A “weak
708 plug” model for Strombolian eruptions. *Earth Planet. Sci. Lett.* 531, 115931.
709 <https://doi.org/10.1016/j.epsl.2019.115931>

710 Parfitt, E.A., 2004. A discussion of the mechanisms of explosive basaltic eruptions. *J. Volcanol.*
711 *Geotherm. Res.* 134, 77–107. <https://doi.org/10.1016/j.jvolgeores.2004.01.002>

712 Patrick, M.R., Harris, A.J.L., Ripepe, M., Dehn, J., Rothery, D.A., Calvari, S., 2007. Strombolian
713 explosive styles and source conditions: Insights from thermal (FLIR) video. *Bull. Volcanol.*
714 69, 769–784. <https://doi.org/10.1007/s00445-006-0107-0>

715 Pering, T.D., McGonigle, A.J.S., James, M.R., Tamburello, G., Aiuppa, A., Delle Donne, D.,
716 Ripepe, M., 2016. Conduit dynamics and post explosion degassing on Stromboli: A combined
717 UV camera and numerical modeling treatment. *Geophys. Res. Lett.* 43, 5009–5016.
718 <https://doi.org/10.1002/2016GL069001>

719 Pichavant, M., Pompilio, M., D'oriano, C., Dicarolo, I., 2011. Petrography, mineralogy and
720 geochemistry of a primitive pumice from Stromboli: implications for the deep feeding system.
721 *Eur. J. Mineral.* 23, 499–517. <https://doi.org/10.1127/0935-1221/2011/0023-2109>

722 Pioli, L., Pistolesi, M., Rosi, M., 2014. Transient explosions at open-vent volcanoes: The case of
723 Stromboli (Italy). *Geology* 42, 863–866. <https://doi.org/10.1130/G35844.1>

724 Pistolesi, M., Donne, D.D., Pioli, L., Rosi, M., Ripepe, M., 2011. The 15 March 2007 explosive
725 crisis at Stromboli volcano, Italy: Assessing physical parameters through a multidisciplinary
726 approach. *J. Geophys. Res. Solid Earth* 116, 1–18. <https://doi.org/10.1029/2011JB008527>

727 Pistolesi, M., Rosi, M., Pioli, L., Renzulli, A., Bertagnini, A., Andronico, D., 2008. The paroxysmal
728 event and its deposits. *Stromboli Volcano An Integr. Study 2002 - 2003 Eruption. Geophysica,*
729 317–330. <https://doi.org/10.1029/182GM26>

730 Polacci, M., Baker, D.R., Mancini, L., Favretto, S., Hill, R.J., 2009. Vesiculation in magmas from
731 Stromboli and implications for normal Strombolian activity and paroxysmal explosions in
732 basaltic systems. *J. Geophys. Res. Solid Earth* 114, 1–14.
733 <https://doi.org/10.1029/2008JB005672>

734 Polacci, M., Corsaro, R.A., Andronico, D., 2006. Coupled textural and compositional
735 characterization of basaltic scoria: Insights into the transition from Strombolian to fire fountain
736 activity at Mount Etna, Italy. *Geology* 34, 201–204. <https://doi.org/10.1130/G22318.1>

737 Pompilio, M., Bertagnini, A., Métrich, N., 2012. Geochemical heterogeneities and dynamics of
738 magmas within the plumbing system of a persistently active volcano: Evidence from
739 Stromboli. *Bull. Volcanol.* 74, 881–894. <https://doi.org/10.1007/s00445-011-0571-z>

740 Ripepe, M., Harris, A.J.L., 2008. Dynamics of the 5 April 2003 explosive paroxysm observed at
741 Stromboli by a near-vent thermal, seismic and infrasonic array. *Geophys. Res. Lett.* 35, 4–9.
742 <https://doi.org/10.1029/2007GL032533>

743 Ripepe, M., Poggi, P., Braun, T., Gordeev, E., 1996. Infrasonic waves and volcanic tremor at
744 Stromboli 23, 181–184.

745 Rosi, M., Bertagnini, A., Harris, A.J.L., Pioli, L., Pistolesi, M., Ripepe, M., 2006. A case history of
746 paroxysmal explosion at Stromboli: Timing and dynamics of the April 5, 2003 event. *Earth
747 Planet. Sci. Lett.* 243, 594–606. <https://doi.org/10.1016/j.epsl.2006.01.035>

748 Rosi, M., Bertagnini, A., Landi, P., 2000. Onset of the persistent activity at Stromboli volcano
749 (Italy). *Bull. Volcanol.* 62, 294–300. <https://doi.org/10.1007/s004450000098>

750 Rosi, M., Pistolesi, M., Bertagnini, A., Landi, P., Pompilio, M., Di Roberto, A., 2013. Chapter 14
751 Stromboli volcano, Aeolian Islands (Italy): present eruptive activity and hazards. *Geol. Soc.
752 London, Mem.* 37, 473–490. <https://doi.org/10.1144/M37.14>

753 Shea, T., Houghton, B.F., Gurioli, L., Cashman, K. V., Hammer, J.E., Hobden, B.J., 2010. Textural
754 studies of vesicles in volcanic rocks: An integrated methodology. *J. Volcanol. Geotherm. Res.*
755 190, 271–289. <https://doi.org/10.1016/j.jvolgeores.2009.12.003>

756 Suckale, J., Keller, T., Cashman, K. V., Persson, P.O., 2016. Flow-to-fracture transition in a
757 volcanic mush plug may govern normal eruptions at Stromboli. *Geophys. Res. Lett.* 43,
758 12,071–12,081. <https://doi.org/10.1002/2016GL071501>

759 Vergnolle, S., Brandeis, G., Mareschal, J., 1996. Strombolian explosions 2. Eruption dynamics
760 determined from acoustic measurements. *J. Geophys. Res.* 101, 20449–20466.
761 <https://doi.org/10.1029/96JB01925> Woitischek, J., Edmonds, M., Woods, A.W., 2020. The

762 control of magma crystallinity on the fluctuations in gas composition at open vent basaltic
763 volcanoes. Scientific Reports 10:14862 <https://doi.org/10.1038/s41598-020-71667-7>

764 Woitischek, J., Edmonds, M., Woods, A.W., 2020. The control of magma crystallinity on the
765 fluctuations in gas composition at open vent basaltic volcanoes. Scientific Reports 10:14862
766 <https://doi.org/10.1038/s41598-020-71667-7>

Figure 1

[Click here to access/download;Figure;Figure_1.pdf](#)

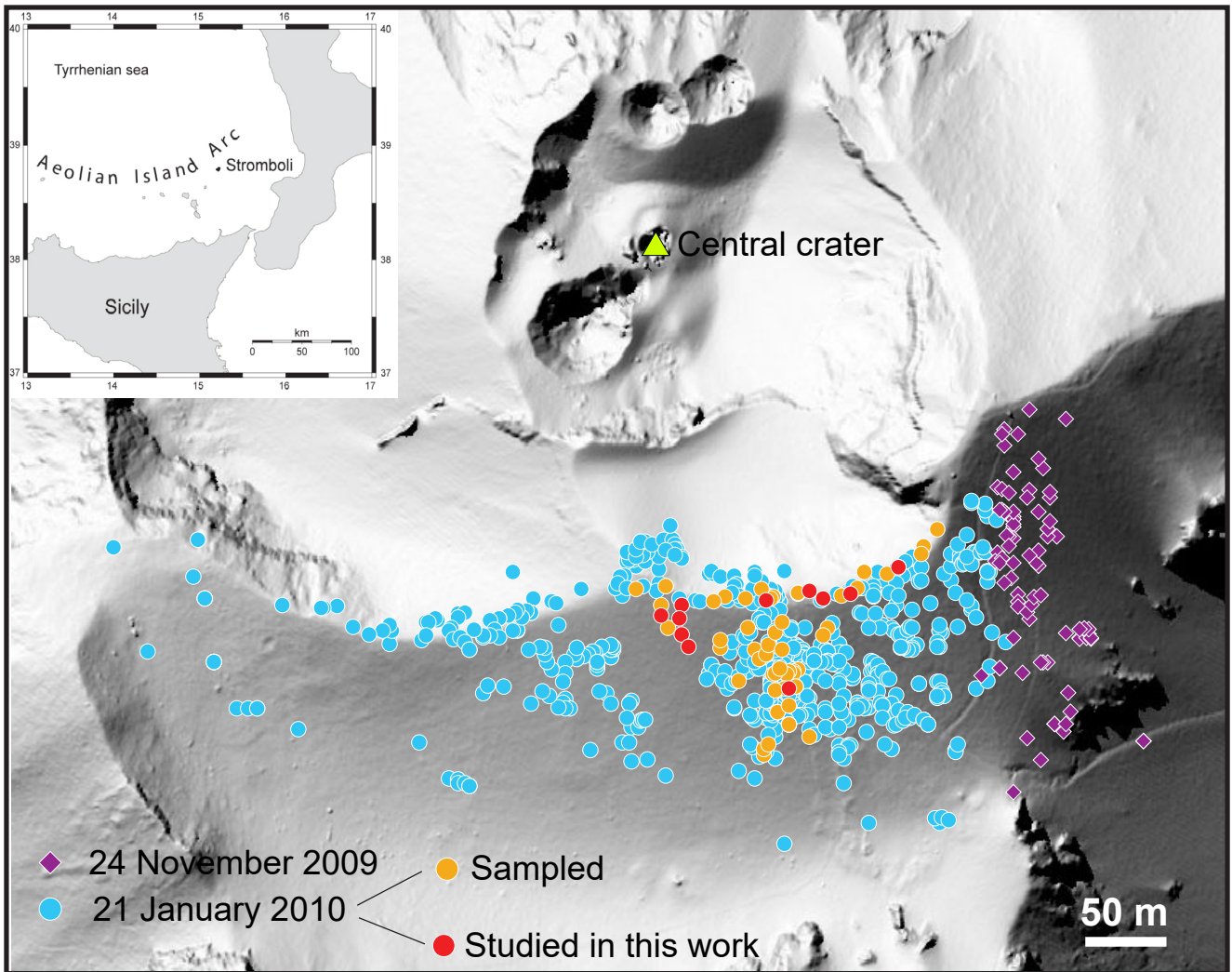


Figure 2

[Click here to access/download;Figure;Figure_2.pdf](#)

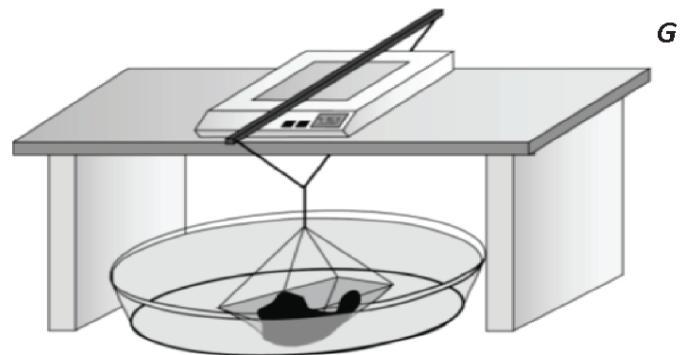
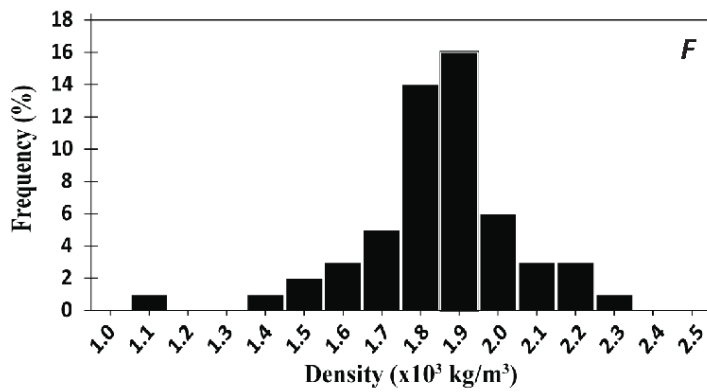
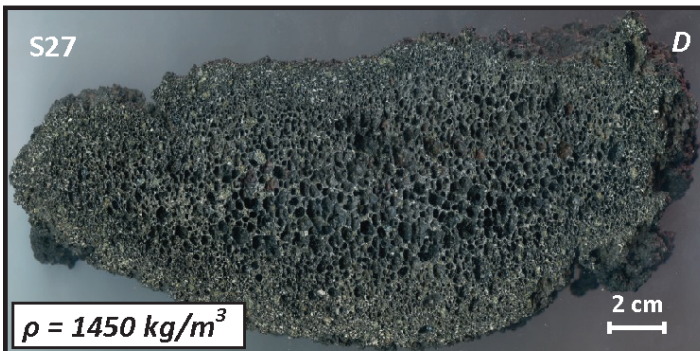
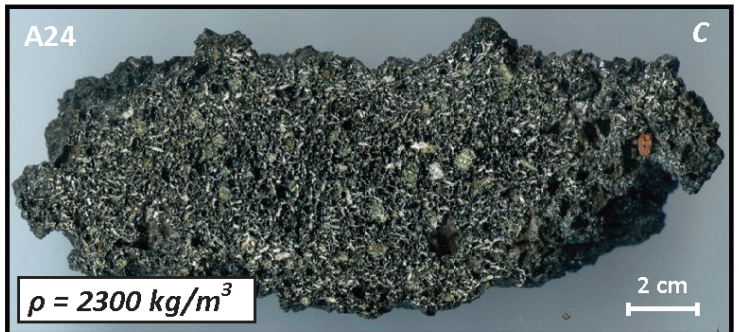
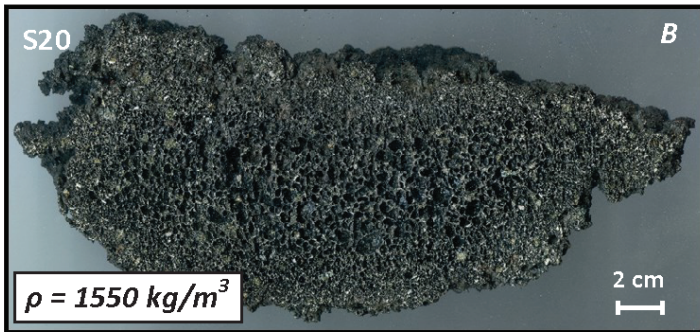
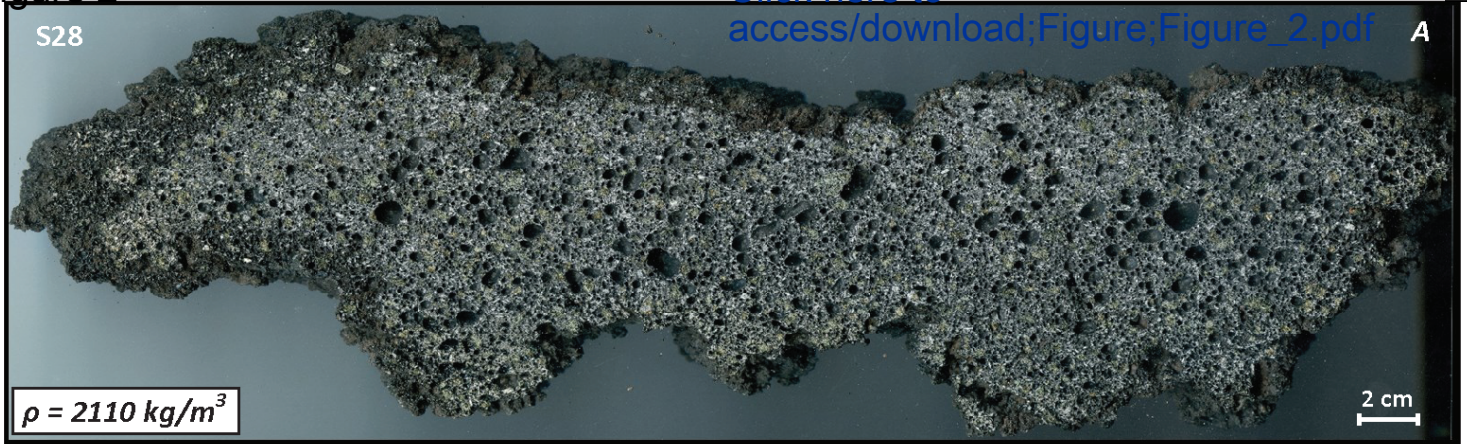
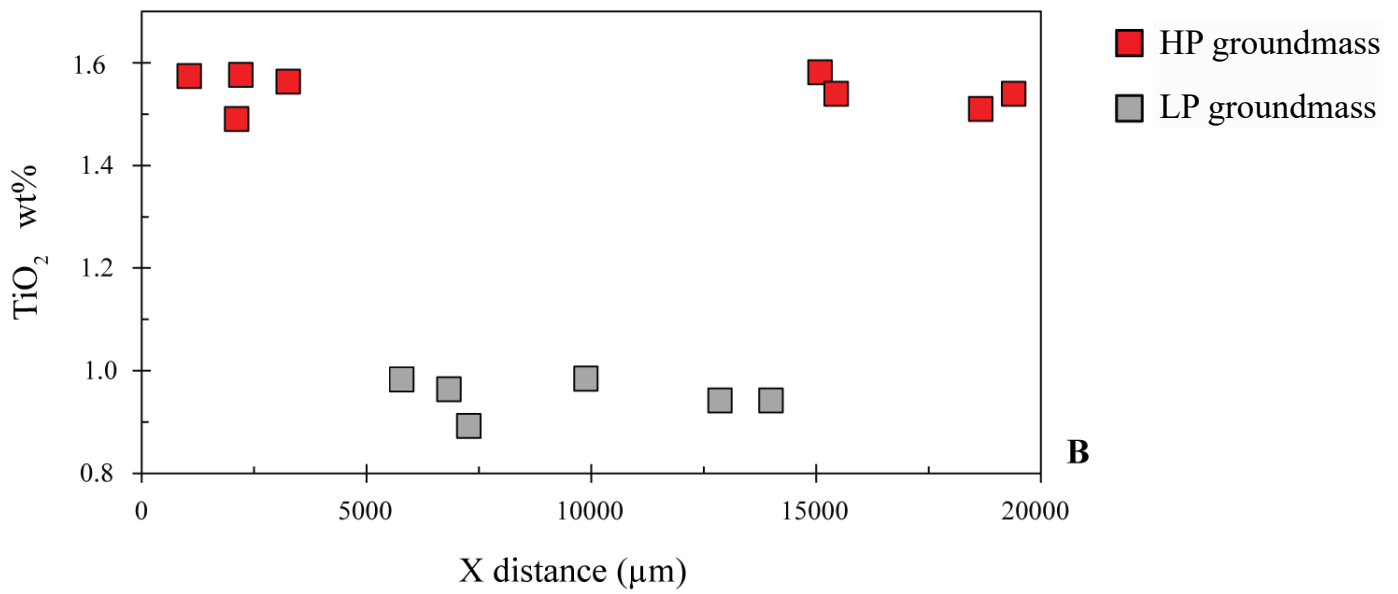
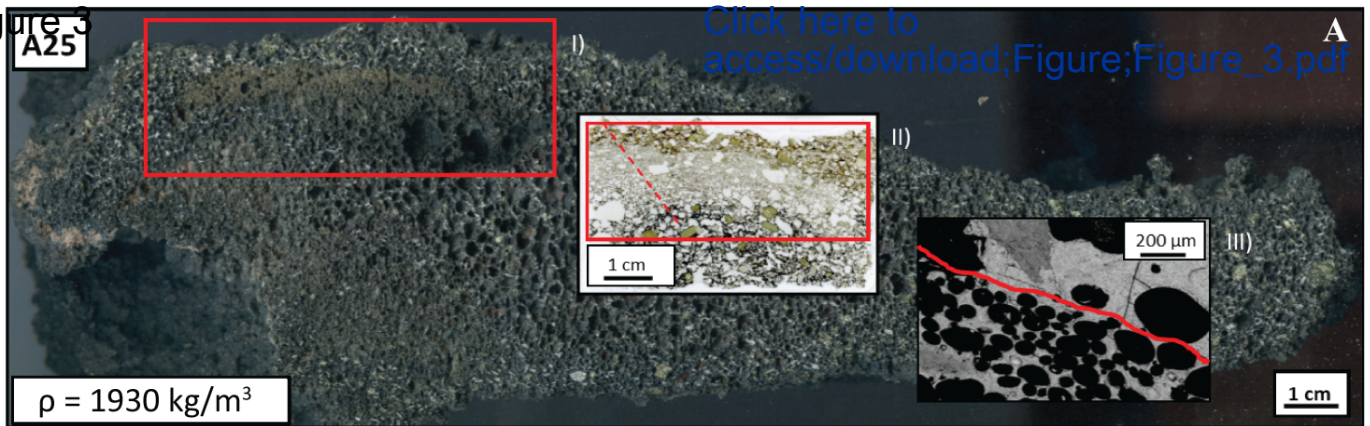


Figure 3



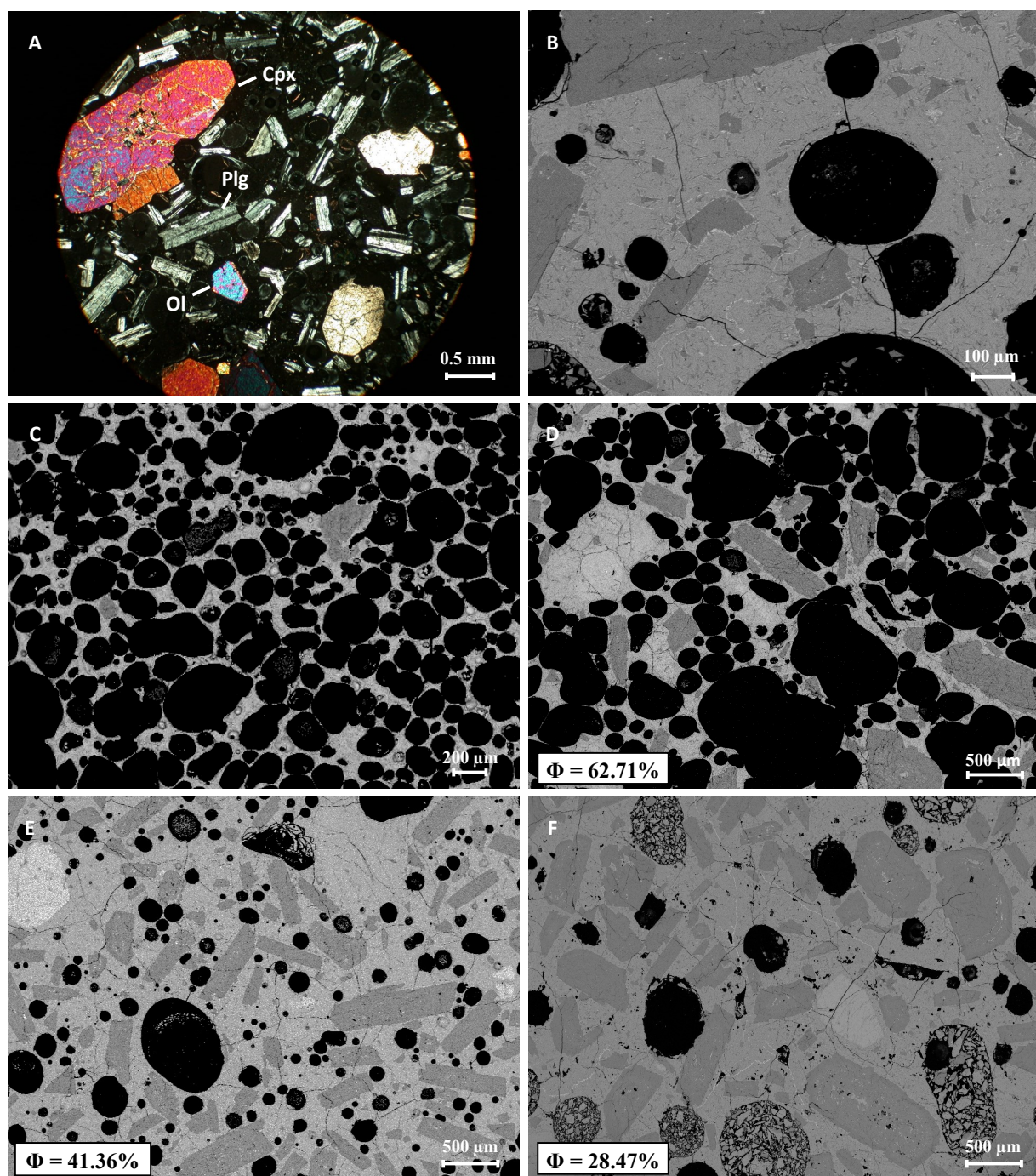
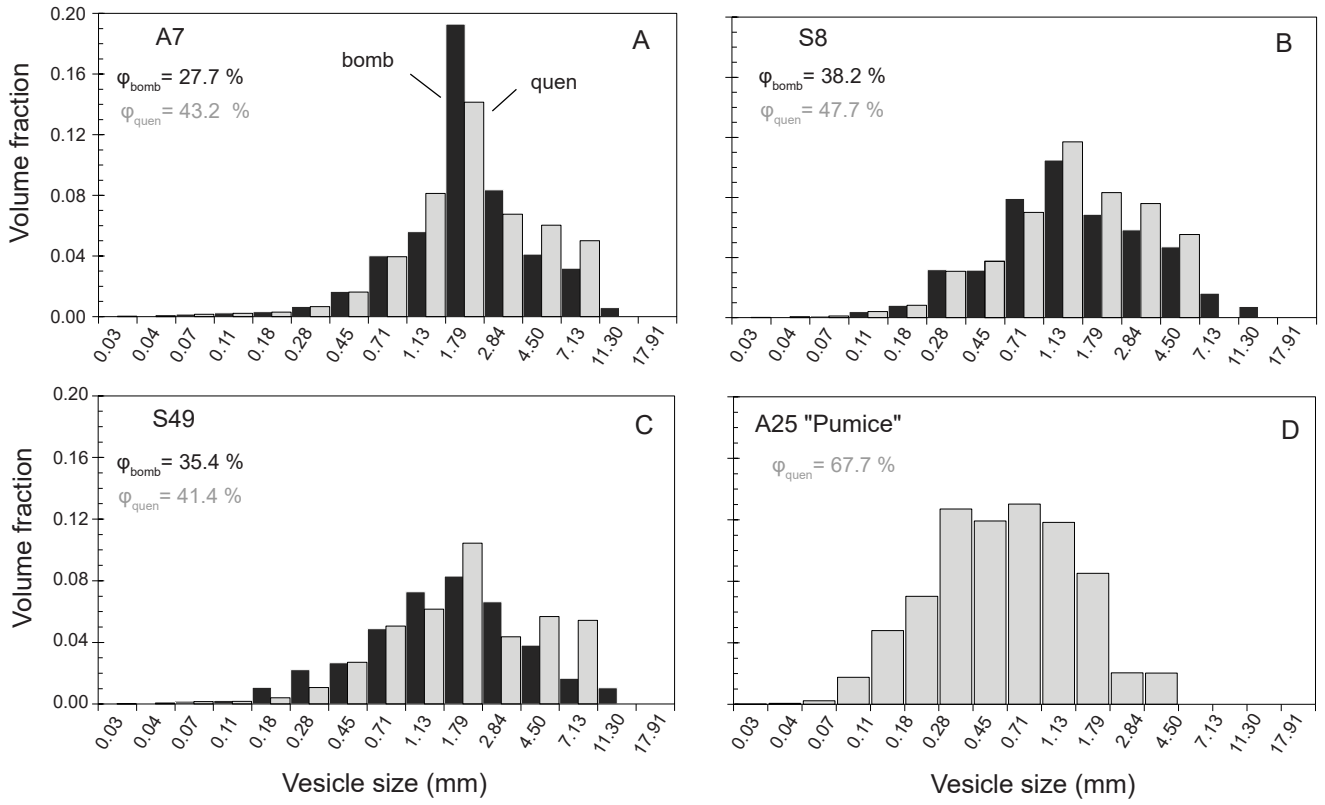


Figure 5



Crystal size distribution (CSDs)

